Model of Faraday waves in a cylindrical container with force detuning ⊕

D. Ding; J. B. Bostwick ✉ iD

Check for updates

View Online

Export Citation

Articles You May Be Interested In

KoopmanLab: Machine learning for solving complex physics equations

APL Mach. Learn. (September 2023)

Experimental realization of a quantum classification: Bell state measurement via machine learning

APL Mach. Learn. (September 2023)

Model of Faraday waves in a cylindrical container with force detuning ⓔⓟ

View Online   Export Citation   CrossMark

D. Ding and J. B. Bostwick[a) ⓘⒹ

AFFILIATIONS

Department of Mechanical Engineering, Clemson University, Clemson, South Carolina 29634, USA

[a)]Author to whom correspondence should be addressed: jbostwi@clemson.edu

ABSTRACT

Recent experiments by Shao *et al.* ["Surface wave pattern formation in a cylindrical container," J. Fluid Mech. **915**, A19 (2021)] have revealed complex wave dynamics on the surface of a liquid bath in a vertically vibrated cylindrical container that are related to the presence of a meniscus on the container sidewall. We develop a corresponding theoretical model for this system by detuning the driving acceleration of the container, which results in an inhomogeneous Mathieu equation that governs the wave dynamics whose spatial structure is defined by the mode number pair (n, m), with n and m the radial and azimuthal mode numbers, respectively. Asymmetric $m \neq 0$ modes are unaffected by the detuning parameter, which is related to the meniscus shape and satisfy a homogeneous Mathieu equation with the shape of the instability tongues computed by the Floquet theory. The Poincaré–Lindstedt method is used to compute the instability tongues for the axisymmetric $m = 0$ modes, which have a lower threshold acceleration and larger bandwidth that depend upon the detuning parameter. Our model results explicitly show how the shape of the meniscus and spatial structure of the wave determine the temporal response and are in good agreement with prior experimental observations for both pure modes and mixed modes.

I. INTRODUCTION

Faraday waves have been synonymous with pattern formation since their discovery by Faraday[2] and have been used in application to redistribute particles[3] and surfactants[4] on thin liquid films, for drop atomization,[5–7] and for the assembly of multiple cell types or organoids into highly complex *in vitro* tissues,[8] to name a few. As summarized by Benjamin and Ursell,[9] there was some dispute in the literature on the temporal response of the interfacial waves formed at the interface of a vertically vibrated liquid bath; Faraday[2] observed that these waves oscillated at a frequency f that was one half of the driving frequency f_d, $f = f_d/2$, or exhibited a subharmonic response, which was later confirmed by Rayleigh,[10] whereas Matthiessen[11,12] reported a harmonic response $f = f_d$. This dispute was resolved by the theoretical analysis of Benjamin and Ursell,[9] who showed that Faraday waves obey a Mathieu equation, which can exhibit both a subharmonic and harmonic response, as well as superharmonic response. Recent experiments by Shao *et al.*[1] in a cylindrical container have shown that the temporal response of the wave is largely determined by its spatial structure, as demonstrated by the observation of (i) harmonic axisymmetric edge waves,[13] (ii) subharmonic asymmetric waves, and (iii) mixed modes which consist of simultaneous excitation of a harmonic

axisymmetric mode with a subharmonic asymmetric mode at a single driving frequency, as shown in Fig. 1. Shao *et al.*[14] have shown that the geometry of the meniscus formed at the container sidewall is critical in determining the temporal wave response; harmonic edge waves are observed at small driving amplitudes with a non-trivial meniscus, but are not observed for a perfectly flat interface with no meniscus. In this paper, we develop a theoretical model of Faraday waves in a cylindrical container that recovers the complex experimental observations of Shao *et al.*[1] described above. This is accomplished by detuning the driving acceleration, which we show is related to the shape of the meniscus.

In general, theoretical analysis of Faraday waves leads to a generalized Mathieu equation

$$\ddot{\boldsymbol{y}} + \boldsymbol{c}\dot{\boldsymbol{y}} + (\boldsymbol{P} - 2A\boldsymbol{Q}\cos f_d t)\boldsymbol{y} = 0, \qquad (1)$$

where P, Q are real-valued parameters, A is the driving amplitude, c is the damping coefficient, and f_d is the driving frequency, as seen in the analysis of Benjamin and Ursell[9] for an inviscid liquid bath, which was later extended by Kumar[15,16] to include viscous effects showing that the resulting system did not give rise to a simple damped Mathieu equation and that this model showed better agreement with the experiments of Edwards and Fauve[17] than the phenomenological-based
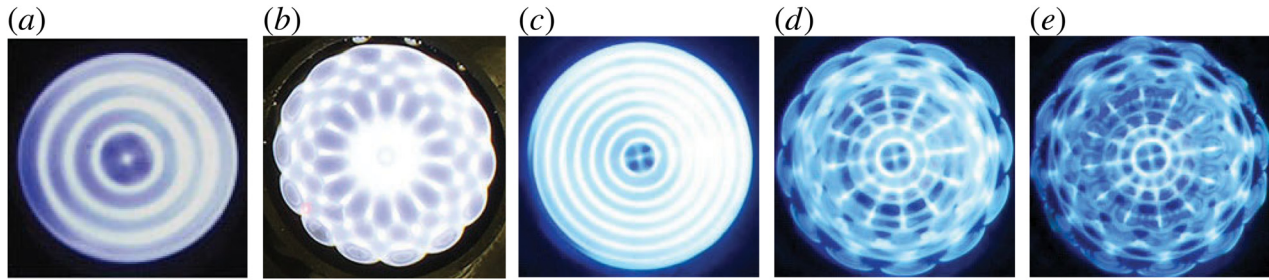
14 November 2024 18:31:10

FIG. 1. Experimentally observed modes of Shao et al.[1] including (a) harmonic axisymmetric mode, (b) subharmonic asymmetric mode, and (d) and (e) mixed mode (right) which corresponds to an axisymmetric harmonic mode (c) that mixes with a subharmonic asymmetric mode (d) and (e) upon increasing the driving amplitude (left to right). Reproduced with permission from Shao et al., J. Fluid Mech. **915**, A19 (2021). Copyright 2021 Cambridge University Press.

damped Mathieu equation. We note that it is challenging to adapt this full theory to the case of a non-trivial meniscus with pinned contact-line. Both of these studies assumed a free contact line condition and resulted in uncoupled equations, whereas Kidambi[18] showed that for an inviscid liquid in a brimful cylinder with pinned contact line condition leads to a coupled Mathieu equation and the phenomena of combination resonance. Typically, the Floquet theory is invoked to solve (1) and gives rise to the instability tongues shown in Fig. 2, which plots the driving amplitude A against the normalized driving frequency f_d/f. In the absence of damping $c = 0$, the subharmonic ($f_d/f = 2$) and harmonic ($f_d/f = 1$) tongues emanate from the frequency axis and have threshold acceleration $A = 0$ at resonance. For parameters (A, f_d) inside the instability tongues, one then observe dynamics with that respective temporal response. Weak damping $c = 0.1$ leads to a non-trivial threshold acceleration $A \neq 0$ that is larger for the harmonic tongue than the subharmonic tongue, which is perhaps the reason why a subharmonic response is more readily observed in experiment, in addition to having a larger bandwidth. However, there are exceptions including the case of thin viscous fluid layers,[16,19] and the previously discussed axisymmetric modes in a cylindrical container.[1] We note
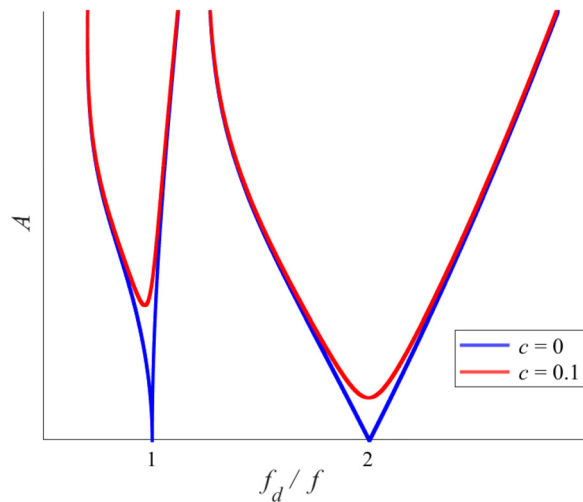

FIG. 2. Instability tongues of the Mathieu equation plotting the driving amplitude A against normalized driving frequency f_d/f contrasting the undamped $c = 0$ case with small damping $c = 0.1$.

that a similar observation occurs in sessile drops, where the axisymmetric modes also exhibit a harmonic response.[20]

In experiment, one typically attempts to enforce a prescribed condition at the contact line, either (i) pinned or (ii) free. To create a pinned contact line requires the liquid to completely fill the container in the "brimful" condition resulting in a contact line that is affixed to the sharp container edge.[1,21] This is a standard approach. However, to create a free contact line requires either the use of high concentrations of soluble surfactants[22] or two or more carefully chosen immiscible liquids.[23] In both cases, the presence of a meniscus can induce harmonic edge waves unless the interface is perfectly, as previously discussed.[14] For large containers (relative to the wavelength)[24] or highly viscous fluids,[25] the edge waves are quickly damped out and do not affect the Faraday wave. In contrast, for small containers the surface wave conforms to the container geometry leading to the coupling of edge waves with parametric waves.[21] Douady[21] suggested that the parametric waves are coupled to the edge waves at second order in a weakly nonlinear analysis, which was recently performed by Bongarzone et al.[26] to predict the onset of viscous Faraday waves in both brimful and nearly brimful cylindrical containers. Bongzarone et al.[26] assumes the additional forcing term appears at second order and, therefore, couples with the parametric waves at third order in a weakly nonlinear analysis focused on the onset of viscous subharmonic standing waves. Our approach is different in that we introduce meniscus effects by "detuning" the driving acceleration, which are readily incorporated into a linear theory, to explain the onset of viscous harmonic waves. This leads to an inhomogeneous Mathieu equation,

$$\ddot{\mathbf{y}} + c\dot{\mathbf{y}} + (\mathbf{P} - 2A\mathbf{Q}\cos f_d t)\mathbf{y} = \mathbf{F}\cos f_d t, \qquad (2)$$

for the axisymmetric modes, where F is the amplitude of periodic forcing, as suggested by Batson et al.,[23,27] that is distinguished by an additional linear forcing term on the right hand side. For asymmetric modes, the governing equation reduces to the standard homogeneous Mathieu equation (1). Floquet theory is appropriate for homogeneous systems but may not work for inhomogeneous systems, and, to our knowledge, no one has analyzed the coupled inhomogeneous Mathieu equation, with the exception of Younesian et al.[28] who suggests a multiple timescale or Poincaré–Lindstedt method. Here, we compute the shape of the instability tongues using the Poincaré–Lindstedt method.

Damping is important, as this affects the threshold acceleration in Faraday waves. Here, damping manifests itself through bulk viscous dissipation, dissipation in the Stokes boundary layer at the container

boundary, and contact line dissipation, each of which has been studied. Henderson and Miles[29] introduced a first order approximation for damping in the Stokes boundary layer and the bulk liquid, which was later extended to higher orders by Martel *et al.*,[30] and considered in a more rigorous way by Muller *et al.*[19] A dynamic contact line can induce dissipation,[31,32] except in the limiting cases of a pinned contact line and free contact line. Kidambi[33] considers the moving contact line case with a meniscus. Here, we consider both free and pinned contact line conditions with a meniscus and introduce linear damping through the viscous potential flow approximation[34] for bulk viscous dissipation, which we feel is a reasonable approximation as our focus is on the coupling between the meniscus wave and parametric wave.

Finally, we note that there is a large volume of literature devoted to complexity in Faraday waves including the experimental observation that two modes, which share nearly the same frequency may interact chaotically[35–37] and quasi-patterns that result when there are multiple driving frequencies in the system.[17,38–40] The complexity we are focused on is the relationship between the meniscus and the spatio-temporal response of the surface wave for a system with a single driving frequency.

We begin this paper by describing our mathematical model of surface waves in a vertically vibrated cylindrical container, which incorporates force detuning that we show is related to the shape of the meniscus and gives rise to a coupled inhomogeneous Mathieu equation. Our analysis explicitly shows how the spatial wave structure and meniscus shape enter the governing equation, allowing us to very easily show that our model recovers essential features of prior experimental results. We then compute the shape of the instability tongues using (i) standard Floquet theory for the homogeneous case and (ii) the Poincare–Lindstedt method for the inhomogeneous case, showing how it depends upon the relevant dimensionless parameters in the problem. We focus on relating our theoretical predictions to the experimental observations described above to both validate our model and better understand the associated physics. The agreement in general is good.

II. MATHEMATICAL FORMULATION

Consider a circular cylinder of radius R filled with a liquid of given volume V that is bound by a static free surface $z = \eta_s(r)$, endowed with a surface tension σ, that forms a static contact angle θ_0 with the container sidewall, as shown in Fig. 3. Here, we consider the large Bond number $Bo = \rho g R^2/\sigma \geq 100$ regime, with ρ the density, and g the gravitational acceleration. The shape of the static interface $\eta_s(r)$ for large Bond number $Bo \geq 100$ is described in Ref. 41, which is given by

$$\eta_s(r) = \xi \delta^{\frac{5}{2}} \frac{\exp(r/\delta)}{(2\pi)^{1/2}} \left[1 + \frac{1}{2}(1-r) + \frac{\delta}{8} + O(\delta^2)\right], \quad (3a)$$

where

$$\delta = Bo^{-1/2}, \quad \xi = e^{-1/\delta}\delta^{-\frac{3}{2}}\lambda_0(1 + \delta\lambda_1 + o(\delta)), \quad (3b)$$

with

$$\lambda_0 = 4(2\pi)^{\frac{1}{2}} \tan\frac{1}{4}\psi_1 \exp\left\{-2\left[1 - \cos\frac{1}{2}\psi_1\right]\right\},$$
$$\lambda_1 = \frac{35}{24} - \cos\frac{1}{2}\psi_1 - \frac{2}{3}\sin^2\frac{1}{2}\psi_1 - \frac{1}{6}\left[1 + \cos\left(\frac{1}{2}\psi_1\right)\right]^{-1} \quad (3c)$$

and $\psi_1 = \frac{1}{2}\pi - \theta_0$. We note that in the large Bond number limit, the interface is essentially flat except near the contact-line region where a meniscus is formed. The liquid depth h is measured from the bottom of the cylinder to the static contact line. The container is subjected to a vertical periodic acceleration a_{tt} along the z axis as defined in a cylindrical coordinate system (r, θ, z). This induces an interface disturbance $\eta(r, \theta, t)$ of size ε and corresponding free surface flow that is described by a velocity field $U(r, z, \theta, t)$ and pressure field $P(r, z, \theta, t)$ that satisfy the continuity and Euler equations,

$$\nabla \cdot U = 0, \quad (4a)$$

$$\rho\left(\frac{\partial}{\partial t} + (U \cdot \nabla)\right)U = -\nabla P - \rho(g - a_{tt})e_z. \quad (4b)$$

At the free surface, the interface shape η is coupled to the flow field through the kinematic condition

$$\frac{\partial \eta}{\partial t} + U \cdot \nabla \eta = U \cdot n \quad (5)$$
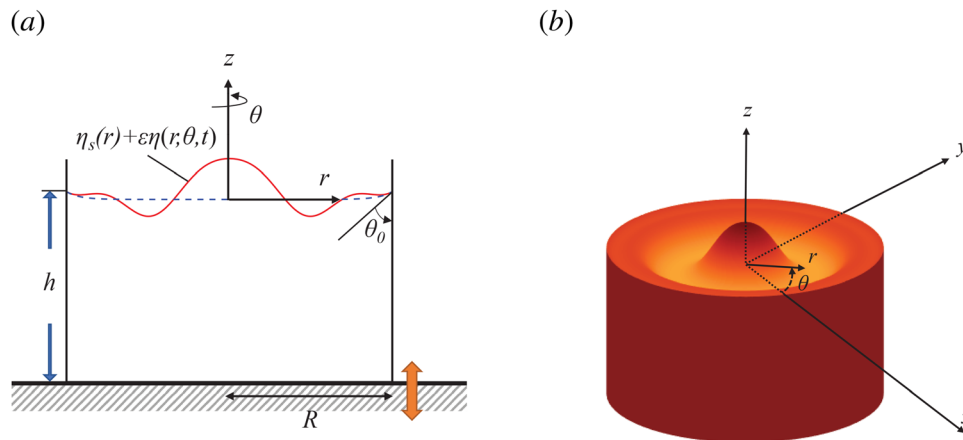
and Young–Laplace equation

(a) *(b)*

FIG. 3. Definition sketch in (a) 2D planar and (b) 3D perspective views.

$$P/\sigma = 2H, \qquad (6)$$

which relates the pressure jump across the interface to the mean curvature H there. Finally, a zero velocity condition is applied on the solid container boundaries

$$\boldsymbol{U} = \boldsymbol{0}|_{r=R, z=\eta_s(R)-h}. \qquad (7)$$

A. Detuning of the driving force

The functional form of the forcing term is critical in determining the temporal response of the liquid. Here, we assume $a_{tt} = g\cos(\omega t)A/R$, where A is the forcing amplitude, and introduce a novel definition of the dimensionless forcing amplitude

$$\chi = A/R = \chi_0 + \varepsilon\chi_1 + \mathcal{O}(\varepsilon^2) \qquad (8)$$

with χ_0 the driving amplitude and χ_1 a detuning parameter. We will show that the effect of the detuning parameter is to cause an excess pressure at first order in our perturbation analysis, which is similar to that proposed by Maksymov et al.[42] to account for a meniscus on a pancake-shaped drop. The idea is that pressure on the interface due to the driving force ρa_{tt} should be related to the shape of the meniscus in a manner that is to be determined. Here, χ_1 can be treated either as a fitting parameter. The detuning approach is typical in nonlinear vibrations, where one often detunes the frequency [cf. Rand, Ref. 43, Eq. (243)] to, e.g., find the transition curves of the Mathieu equation. However, we take a different approach by detuning the forcing amplitude for the reasons mentioned above, which leads to the detuning parameter χ_1.

B. Linearized equations

We introduce the *ad hoc* base-state for Eqs. (4)–(7) as

$$\hat{\boldsymbol{U}} = 0, \quad \hat{P}(z,t) = -\rho g(1 - \chi_0\cos\omega t)z + C(t), \qquad (9)$$

where $C(t)$ is independent of the spatial variable. We perform a linear stability analysis about this base-state by decomposing the velocity and pressure fields as

$$\boldsymbol{U} = \hat{\boldsymbol{U}} + \varepsilon\boldsymbol{u} = \varepsilon\nabla\phi, \quad P = \hat{P} + \varepsilon p, \qquad (10)$$

where we have assumed an irrotational flow described by the velocity potential ϕ. Substituting (10) into (4) and collecting the $\mathcal{O}(\varepsilon)$ terms gives

$$\nabla^2\phi = 0, \qquad (11a)$$

$$p = -\rho\frac{\partial\phi}{\partial t} + \chi_1\rho gz\cos\omega t. \qquad (11b)$$

Similarly, the kinematic condition (5) reduces to

$$\frac{\partial\phi}{\partial z} = \frac{\partial\eta}{\partial t} + \frac{\partial\phi}{\partial r}\frac{d\eta_s(r)}{dr} \qquad (12)$$

and the no-penetration condition (7) reduces to

$$\left.\frac{\partial\phi}{\partial r}\right|_{r=R} = 0, \quad \left.\frac{\partial\phi}{\partial z}\right|_{z=\eta_s(R)-h} = 0. \qquad (13)$$

The Young–Laplace equation (6) can be written as

$$P|_{z=\eta_s(r)+\varepsilon\eta} - 2\mu\frac{\partial^2\phi}{\partial z^2} \approx \hat{P}|_{z=\eta_s(r)} + \varepsilon p|_{z=\eta_s(r)}$$

$$+ \varepsilon\eta\left(\frac{\partial\hat{P}}{\partial z}\right)\bigg|_{z=\eta_s(r)} - 2\mu\frac{\partial^2\phi}{\partial z^2}$$

$$= \sigma(\nabla\cdot\boldsymbol{n})_{z=\eta_s+\varepsilon\eta} \qquad (14)$$

with $\hat{P}|_{z=\eta_s(r)} = \sigma(\nabla\cdot\boldsymbol{n})_{z=\eta_s}$ and $p|_{z=\eta_s(r)} = -\rho\frac{\partial\phi}{\partial t} + \rho g\chi_1\cos\omega t\eta_s(r)$. Here, we have applied viscous potential flow[34] to approximate the bulk viscous dissipation and introduce a linear damping term into the problem. We note that other sources of damping including the viscous boundary layer at the solid substrate, dissipation associated with a moving contact line, and the viscous correction of the viscous potential flow theory due to the solenoidal component of the velocity,[44] all of which would similarly introduce linear damping terms that could be combined into a lumped parameter model of linear damping. We note that viscous effects due to vorticity are often confined to a boundary layer and are often smaller than those due to irrotational flow,[45] and the dissipation near the bottom of the container is negligible especially when the depth of the container is large enough.[46,47] Given that our focus is not on the energy budget and differentiating the various forms of dissipation from one another, the viscous potential flow approximation is a reasonable one.

C. Reduced equations

Dimensionless variables,

$$r^* = r/R, \quad z^* = z/R, \quad h^* = h/R, \quad t^* = \frac{t}{\sqrt{R/g}}, \quad \phi^* = \frac{\phi}{\sqrt{R^3 g}} \qquad (15)$$

and dimensionless numbers

$$Bo = \frac{\rho g R^2}{\sigma}, \quad Ga = \frac{g\rho^2 R^3}{\mu^2} \qquad (16)$$

are introduced, where Bo is the Bond number and Ga is the Galilei number. Normal modes

$$\eta = \eta^*(r,t)e^{im\theta}, \quad \phi = \phi^*(r,z,t)e^{im\theta} \qquad (17)$$

are applied with m the azimuthal mode number. Herein, we drop the $*$ and refer to dimensionless quantities. A standard manipulation of the field equations in which the problem is mapped to the boundary (i.e., boundary integral approach[48,49]) results in the following governing equation:

$$\frac{\partial\phi}{\partial t} + 2Ga^{-\frac{1}{2}}\frac{\partial^2\phi}{\partial z^2} - \frac{1}{Bo}k[\eta] + (1 - \chi_0\cos\omega t)\eta$$
$$= \delta_{0,m}\chi_1\eta_s(r)\cos\omega t, \qquad (18)$$

where

$$k[\eta] = \Xi(r)\frac{\partial^2\eta}{\partial r^2} + q(r)\frac{\partial\eta}{\partial r} - m^2 w(r)\frac{1}{r^2}\eta \qquad (19)$$

with

$$\Xi(r) = \frac{1}{(1+\eta_s'^2)^{3/2}}, \quad q(r) = \frac{1+3\eta_s'^2}{r(1+\eta_s'^2)^{3/2}} - \frac{3\eta_s'k_s}{(1+\eta_s'^2)},$$

$$w(r) = \frac{1}{(1+\eta_s'^2)^{1/2}}, \quad k_s = \frac{\eta_s'' + \eta_s'(1+\eta_s'^2)/r}{(1+\eta_s'^2)^{3/2}}. \tag{20}$$

Here, $\delta_{0,m}$ is the Kronecker delta with $\delta_{0,0}=1$, $\delta_{0,m\neq0}=0$, and ′ indicates d/dr. The most important thing to note here is that the force detuning effect is trivial for a perfectly flat interface $\eta_s = 0$.

Equation (18) is augmented with a contact line boundary condition, which we assume to be either pinned or free to move,

$$\eta|_{r=1} = 0, \quad \text{Pinned condition;}$$

$$\left.\frac{\partial\eta}{\partial r}\right|_{r=1} = 0, \quad \text{Free condition,} \tag{21}$$

and an integral condition

$$\int_0^1 r\eta(r,t)dr = 0 \tag{22}$$

necessary to ensure volume conservation for the axisymmetric $m = 0$ modes. Note that the asymmetric modes $m \neq 0$ naturally satisfy volume conservation.

D. Derivation of inhomogeneous Mathieu equation

We seek a solution (η, ϕ) to the governing equations (12), (13), (18), (21), and (22) in the form

$$\eta(r,t) = \sum_{n=1}^{\infty} a_n(t)V_n^m(r),$$

$$\phi(r,z,t) = \sum_{n=1}^{\infty} b_n(t)\frac{\cosh k_{mn}(z+h-\eta_s(1))}{\sinh k_{mn}h}J_m(k_{mn}r), \tag{23}$$

where k_{mn} is the nth zero of $J_m'(k)$ as required to satisfy the no-penetration condition at the container sidewall $r = 1$ (13). Here, V_n^m are a set of orthonormal basis functions chosen to satisfy the contact line (21) and integral (22) conditions. For the free contact line condition,

$$V_n^m(r) = J_m(k_{mn}r), \tag{24}$$

or a set of Bessel functions. The pinned contact line condition is not as straightforward as it is not compatible with the no-penetration condition on the lateral support. This can be accounted for by defining a set of basis functions that satisfy the pinned contact line condition,

$$S_n^m(r) = J_m(k_{mn}r) - \frac{J_m(k_{mn})}{J_m(k_{m1})}J_m(k_{m1}r), \quad n = 2,3,\dots N, \tag{25}$$

and applying the Gram–Schmidt procedure to deliver an orthonormal set of basis functions $V_n^m(r)$, where $n = 1,2,3,\dots N$. This approach has been applied to similar problems by Bostwick and Steen[50] and Wilson et al.[51]

Substituting (23) into (12) and (18) gives

$$\sum_{n=1}^{\infty}\left(\frac{da_n}{dt}V_n^m(r) - b_n k_{mn}\frac{\sinh k_{mn}(\eta_s(r)+h-\eta_s(1))}{\sinh k_{mn}h}J_m(k_{mn}r)\right.$$

$$\left. + b_n\eta_s'(r)\frac{\cosh k_{mn}(\eta_s(r)+h-\eta_s(1))}{\sinh k_{mn}h}\frac{dJ_m(k_{mn}r)}{dr}\right) = 0, \tag{26a}$$

$$\sum_{n=1}^{\infty}\left(\frac{db_n}{dt}\frac{\cosh k_{mn}(\eta_s(r)+h-\eta_s(1))}{\sinh k_{mn}h}J_m(k_{mn}r)\right.$$

$$+ 2Ga^{-\frac{1}{2}}b_n k_{mn}^2\frac{\cosh k_{mn}(\eta_s(r)+h-\eta_s(1))}{\sinh k_{mn}h}J_m(k_{mn}r)$$

$$\left. + a_n(1-\chi_0\cos\omega t)V_n^m(r) - \frac{1}{Bo}a_n k^*\left[V_n^m(r)\right]\right)$$

$$= \delta_{0,m}\chi_1\cos\omega t\eta_s(r), \tag{26b}$$

respectively.

Projecting (26a) onto the function space $\{V_\ell^m(r)\}, \ell = 1,2,\dots N$, via the inner product $\langle f,g \rangle = \int_0^1 rf(r)g(r)dr$, we obtain

$$b_n = \sum_{\ell=1}^{N}\beta_{n\ell}\frac{da_\ell}{dt} \tag{27}$$

with

$$\beta_{n\ell} = \left(\int_0^1 r\left((k_{mn}\frac{\sinh k_{mn}(\eta_s(r)+h-\eta_s(1))}{\sinh k_{mn}h}J_m(k_{mn}r)\right.\right.$$

$$\left.\left. - \eta_s'(r)\frac{\cosh k_{mn}(\eta_s(r)+h-\eta_s(1))}{\sinh k_{mn}h}\frac{dJ_m(k_{mn}r)}{dr}\right)V_\ell^m(r)dr\right)^{-1}. \tag{28}$$

Similarly, we project (26b) onto $\{V_p^m(r)\}, p = 1,2,\dots N$, and use (27) to obtain a system of N coupled second-order ODEs

$$\sum_{n=1}^{N}\gamma_{pn}\sum_{\ell=1}^{N}\beta_{n\ell}\frac{d^2a_\ell}{dt^2} + 2Ga^{-\frac{1}{2}}\sum_{n=1}^{N}K_{pn}\sum_{\ell=1}^{N}\beta_{n\ell}\frac{da_\ell}{dt}$$

$$+ a_p(1-\chi_0\cos\omega t) - \sum_{n=1}^{N}H_{pn}a_n$$

$$= \delta_{0,m}\chi_1\hat{\tau}_p\cos\omega t, \quad p = 1,2,\dots,N, \tag{29}$$

with

$$\gamma_{pn} = \int_0^1 r\frac{\cosh k_{mn}(\eta_s(r)+h-\eta_s(1))}{\sinh k_{mn}h}J_m(k_{mn}r)V_p^m(r)dr, \tag{30a}$$

$$K_{pn} = \int_0^1 rk_{mn}^2\frac{\cosh k_{mn}(\eta_s(r)+h-\eta_s(1))}{\sinh k_{mn}h}J_m(k_{mn}r)V_p^m(r)dr, \tag{30b}$$

$$H_{pn} = \frac{1}{Bo}\int_0^1 rk\left[V_n^m(r)\right]V_p^m(r)dr, \tag{30c}$$

$$\hat{\tau}_p = \int_0^1 r\eta_s(r)V_p^m(r)dr. \tag{30d}$$

Equation (29) can be written in a more compact matrix form

$$\boldsymbol{A}\frac{d^2\boldsymbol{y}}{dt^2} + 2Ga^{-\frac{1}{2}}\hat{\boldsymbol{B}}\frac{d\boldsymbol{y}}{dt} + (\hat{\boldsymbol{P}} - 2\hat{\boldsymbol{Q}}\cos\omega t)\boldsymbol{y} = \delta_{0,m}\chi_1\hat{\boldsymbol{\tau}}\cos\omega t, \tag{31}$$

where $\boldsymbol{y} = (a_1, a_2, \dots, a_N)$ is a coefficient vector and the components of the matrices $\boldsymbol{A}, \hat{\boldsymbol{B}}, \hat{\boldsymbol{P}}$ and $\hat{\boldsymbol{Q}}$ are given by

14 November 2024 18:31:10

$$A_{ij} = \sum_{\ell=1}^{N} \gamma_{i\ell}\beta_{\ell j}, \quad \hat{B}_{ij} = \sum_{\ell=1}^{N} K_{i\ell}\beta_{\ell j},$$

$$\hat{P}_{ij} = -H_{ij} + \begin{cases} 1, & \text{if } i = j. \\ 0, & \text{if } i \neq j. \end{cases}, \quad \hat{Q}_{ij} = \begin{cases} \chi_0/2, & \text{if } i = j. \\ 0, & \text{if } i \neq j. \end{cases} \tag{32}$$

III. SOLUTION METHOD

Equation (31) is readily recognized as an inhomogeneous Mathieu equation and before proceeding further with the analysis it will be instructive to discuss its structure. Note that the right-hand side of Eq. (31) vanishes in the following limiting cases; (1) for asymmetric $m \neq 0$ modes and (2) for a flat meniscus $\eta_s = 0$, equivalently $\tau = 0$, reducing the problem to a homogeneous Mathieu equation that we will solve using the Floquet theory in the standard way. For the special case of the axisymmetric $m = 0$ modes with a non-trivial meniscus $\eta_s \neq 0$, the resulting equation is an inhomogeneous Mathieu equation, which we will solve using a perturbation method.

To facilitate a solution for both of our analytical methods, we rescale (31) by defining $T = \omega t/2$, $\boldsymbol{B} = 2\boldsymbol{A}^{-1}\hat{\boldsymbol{B}}$, $\boldsymbol{P} = 4\boldsymbol{A}^{-1}\hat{\boldsymbol{P}}$, $\boldsymbol{Q} = \frac{4\boldsymbol{A}^{-1}\hat{\boldsymbol{Q}}}{\chi_0}$, $\boldsymbol{\tau} = 4\boldsymbol{A}^{-1}\hat{\boldsymbol{\tau}}$, which gives

$$\omega^2 \frac{d^2\boldsymbol{y}}{dT^2} + 2\omega Ga^{-\frac{1}{2}}\boldsymbol{B}\frac{d\boldsymbol{y}}{dT} + (\boldsymbol{P} - 2\chi_0\boldsymbol{Q}\cos 2T)\boldsymbol{y}$$
$$= \delta_{0,m}\chi_1\boldsymbol{\tau}\cos 2T. \tag{33}$$

A. Floquet theory

The standard way to apply the Floquet theory is to compute the Floquet multipliers to determine the stability using the technique of mapping at a period[52] or Hill's infinite determinant method.[53] Our interest is in the shape of the instability tongues and we follow the method suggested by Kumar *et al.*[15] by fixing the values of the Floquet exponent to trace the stability boundaries for both harmonic and subharmonic tongues. In general, this is a much more computational efficient method.

We begin by seeking a solution to the homogeneous Mathieu equation, i.e., Eq. (33) with right-hand side zero, in the following form:

$$\boldsymbol{y}(T) = e^{\zeta T}\left(\sum_{l=-L}^{L} \boldsymbol{\xi}_l e^{i2lT}\right) \tag{34}$$

with $\boldsymbol{\xi}_l$ a vector with components ξ_l^n, $n = 1, \dots N$. Substituting (34) into (33) gives

$$\sum_{l=-L}^{l=L} \left(\omega^2(\zeta + i2l)^2 \xi_l^n + 2\omega Ga^{-\frac{1}{2}}(\zeta + i2l)\sum_{j=1}^{N}(B_{nj})\xi_l^j \right.$$
$$\left. + \sum_{j=1}^{N}(P_{nj} - 2\chi_0 Q_{nj}\cos 2T)\xi_l^j \right) = 0.$$

Since the range of χ_0 in our stability diagrams is much smaller than the range of ω, we fix χ_0 instead of ω for computational efficiency.[15] For a given χ_0, we can compute the stability boundary by setting $\zeta = 0$ for the harmonic case and $\zeta = i$ for the subharmonic case and solving for the unknown ω from the generalized eigenvalue problem,

$$(\boldsymbol{M}\omega^2 + \boldsymbol{V}\omega + \boldsymbol{W})\boldsymbol{v} = 0, \quad \text{where} \quad \boldsymbol{v} = (\xi_{-L}^1, \xi_{-L+1}^1, \dots, \xi_{L-1}^1, \xi_L^1,$$
$$\xi_{-L}^2, \dots, \xi_{L-1}^N, \xi_L^N)^T.$$

B. Perturbation method

For the axisymmetric $m = 0$ modes, we use the Poincaré–Lindstedt method[54,55] to determine the stability boundaries of the inhomogeneous Mathieu equation. We begin by substituting $\omega = \omega_0 + \chi_0\omega_1 + \chi_0^2\omega_2 + \cdots$, $y_n(T) = y_{n_0}(T) + \chi_0 y_{n_1}(T) + \chi_0^2 y_{n_2}(T) + \cdots$ where $n = 1, 2, \dots, N$ into (33). The meniscus waves are not generated by the parametric resonance, and for small driving amplitude χ_0, it can be well described by a purely linear response, and the meniscus-wave amplitude is proportional to the external forcing amplitude.[26] Therefore, we assume, $\chi_1\boldsymbol{\tau} = \chi_0\boldsymbol{f}$. We should also note that typically the damping term is assumed to be $Ga^{-\frac{1}{2}} = \chi_0\mu$ for the subharmonic response and $Ga^{-\frac{1}{2}} = \chi_0^2\mu$ for the harmonic response with the homogeneous Mathieu equation; however, the inhomogeneous Mathieu equation leads to the possibility that $Ga^{-\frac{1}{2}} = \chi_0\mu$ even for the harmonic tongue. Therefore, we assume $Ga^{-\frac{1}{2}} = \chi_0\mu$ for both subharmonic and harmonic responses and expand in the perturbation parameter χ_0 to give

$$\mathscr{O}(1): \omega_0^2 \frac{d^2 y_{n_0}}{dT^2} + \sum_{i=1}^{N} P_{ni}y_{i_0} = 0, \tag{35a}$$

$$\mathscr{O}(\chi_0): \omega_0^2 \frac{d^2 y_{n_1}}{dT^2} + \sum_{i=1}^{N} P_{ni}y_{i_1} = f_n\cos 2T - 2\sum_{i=1}^{N} Q_{ni}y_{i_0}\cos 2T$$
$$- 2\omega_0\omega_1\frac{d^2 y_{n_0}}{dT^2} - 2\mu\omega_0\sum_{i=1}^{N} B_{ni}\frac{dy_{i_0}}{dT}, \tag{35b}$$

$$\mathscr{O}(\chi_0^2): \omega_0^2\frac{d^2 y_{n_2}}{dT^2} + \sum_{i=1}^{N} P_{ni}y_{i_2}$$
$$= -2\sum_{i=1}^{N} Q_{ni}y_{i_1}\cos 2T - 2\omega_0\omega_1\frac{d^2 y_{n_1}}{dT^2}$$
$$- (2\omega_0\omega_2 + \omega_1^2)\frac{d^2 y_{n_0}}{dT^2}. \tag{35c}$$

1. Subharmonic response

To determine the transition curves for the subharmonic tongues at $\mathscr{O}(1)$, we let $y_{n_0} = C_n e^{iT}$ be the solution of (35a) and solve the eigenvalue problem

$$\omega_0^2\boldsymbol{C} = \boldsymbol{P}\boldsymbol{C}, \tag{36}$$

for the N eigenvalues ω_0 with associated eigenvectors $\boldsymbol{c}$. To remove the secular terms at $\mathscr{O}(\chi_0)$ requires

$$-\sum_{i=1}^{N} Q_{ni}C_i + 2\omega_0\omega_1 C_n - 2i\mu\omega_0\sum_{i=1}^{N} B_{ni}C_i = 0, \tag{37a}$$

$$i\sum_{i=1}^{N} Q_{ni}C_i + 2i\omega_0\omega_1 C_n + 2\mu\omega_0\sum_{i=1}^{N} B_{ni}C_i = 0. \tag{37b}$$

To determine ω_1 associated with the particular ω_0, we project $\boldsymbol{Q}$ and $\boldsymbol{C}$ onto the eigenvector $\boldsymbol{c}$ associated with the eigenvalue ω_0 that was computed at $\mathscr{O}(1)$. This allows us to rewrite (37) as

14 November 2024 18:31:10

$$-\boldsymbol{c}^T \boldsymbol{Q} \boldsymbol{c} \boldsymbol{c}^T \boldsymbol{C} + 2\omega_0 \omega_1 \boldsymbol{c}^T \boldsymbol{C} - 2i\mu\omega_0 \boldsymbol{c}^T \boldsymbol{B} \boldsymbol{c} \boldsymbol{c}^T \boldsymbol{C} = 0, \qquad (38a)$$

$$i\boldsymbol{c}^T \boldsymbol{Q} \boldsymbol{c} \boldsymbol{c}^T \boldsymbol{C} + 2i\omega_0 \omega_1 \boldsymbol{c}^T \boldsymbol{C} + 2\mu\omega_0 \boldsymbol{c}^T \boldsymbol{B} \boldsymbol{c} \boldsymbol{c}^T \boldsymbol{C} = 0, \qquad (38b)$$

from which we can easily determine

$$\omega_1 = \pm \frac{1}{2\omega_0} \sqrt{(\boldsymbol{c}^T \boldsymbol{Q} \boldsymbol{c})^2 - 4\mu^2 \omega_0^2 (\boldsymbol{c}^T \boldsymbol{B} \boldsymbol{c})^2}, \qquad (39)$$

for each $\mathscr{O}(1)$ eigenvalue ω_0 and eigenvector $\boldsymbol{c}$ combination. This then gives the equation for the subharmonic stability tongue,

$$\omega = \omega_0 \pm \frac{1}{2\omega_0} \sqrt{\chi_0^2 (\boldsymbol{c}^T \boldsymbol{Q} \boldsymbol{c})^2 - 4(Ga^{-\frac{1}{2}})^2 \omega_0^2 (\boldsymbol{c}^T \boldsymbol{B} \boldsymbol{c})^2}, \qquad (40)$$

which does not exhibit a dependence on the linear forcing term (right-hand side of inhomogeneous Mathieu equation). We trace the boundary of subharmonic tongue at the order of χ_0 like the classical homogeneous Mathieu equation in perturbation theory.[56]

2. Harmonic response

For the harmonic tongues, we apply an identical procedure by assuming $y_{n_0} = C_n e^{i2T} = E_n \cos 2T + F_n \sin 2T$ to be the solution of (35a) and solve the associated eigenvalue problem to get the eigenvalues ω_0 and corresponding eigenvectors $\boldsymbol{c}$. To remove the secular terms at $\mathscr{O}(\chi_0)$ requires

$$8\omega_0 \omega_1 E_n - 4\mu\omega_0 (B_{n1}F_1 + B_{n2}F_2 + \cdots + B_{nN}F_N) + f_n = 0, \qquad (41a)$$

$$8\omega_0 \omega_1 F_n + 4\mu\omega_0 (B_{n1}E_1 + B_{n2}E_2 + \cdots + B_{nN}E_N) = 0. \qquad (41b)$$

Like the subharmonic case, we project onto the corresponding eigenvectors and determine

$$\omega_1 = \pm \frac{1}{8\omega_0} \sqrt{\frac{(F_c^2 + E_B^2)(\boldsymbol{c}^T \boldsymbol{f})^2}{(E_c E_B + F_c F_B)^2} - 16\mu^2 \omega_0^2}, \qquad (42)$$

where $E_c = \boldsymbol{c}^T \boldsymbol{E}$, $E_B = \boldsymbol{c}^T \boldsymbol{B} \boldsymbol{c} \boldsymbol{c}^T \boldsymbol{E}$, $F_c = \boldsymbol{c}^T \boldsymbol{F}$, $F_B = \boldsymbol{c}^T \boldsymbol{B} \boldsymbol{c} \boldsymbol{c}^T \boldsymbol{F}$. Here, we introduce the dimensionless empirical parameter $(f^*)^2 = \frac{(F_c^2 + E_B^2)(\boldsymbol{c}^T \boldsymbol{f})^2}{(E_c E_B + F_c F_B)^2}$ that is a measure of the harmonic wave amplitude normalized by the response amplitude. The physical interpretation is more clear when the system is uncoupled, $(f^*)^2 = (f/R_A)^2$, where $R_A^2 = E_1^2 + F_1^2$, such that f^* is the inverse of the scaled linear response. We will discuss the interpretation of f^* in Sec. IV. The particular solution $\boldsymbol{y}_{1p}$ is given by

$$\boldsymbol{y}_{1p} = -\frac{1}{4\omega_0^2} \boldsymbol{Q} \boldsymbol{E} + \frac{1}{12\omega_0^2} \boldsymbol{Q} \boldsymbol{E} \cos 4T + \frac{1}{12\omega_0^2} \boldsymbol{Q} \boldsymbol{F} \sin 4T. \qquad (43)$$

To remove the secular terms at $\mathscr{O}(\chi_0^2)$ requires

$$4\omega_1^2 \boldsymbol{E} + 8\omega_0 \omega_2 \boldsymbol{E} + \frac{5}{12\omega_0^2} \boldsymbol{Q} \boldsymbol{Q} \boldsymbol{E} = 0, \qquad (44a)$$

$$4\omega_1^2 \boldsymbol{F} + 8\omega_0 \omega_2 \boldsymbol{F} - \frac{1}{12\omega_0^2} \boldsymbol{Q} \boldsymbol{Q} \boldsymbol{F} = 0. \qquad (44b)$$

We project onto the corresponding eigenvectors and get

$$\omega_2 = \frac{1}{8\omega_0} \left(\frac{1}{12\omega_0^2} (\boldsymbol{c}^T \boldsymbol{Q} \boldsymbol{c})^2 - 4\omega_1^2 \right) \qquad (45a)$$

and

$$\omega_2 = \frac{1}{8\omega_0} \left(\frac{-5}{12\omega_0^2} (\boldsymbol{c}^T \boldsymbol{Q} \boldsymbol{c})^2 - 4\omega_1^2 \right). \qquad (45b)$$

The shape of the harmonic tongue is then given by

$$\omega = \omega_0 + \frac{1}{8\omega_0} \sqrt{\chi_0^2 (f^*)^2 - 16(Ga^{-\frac{1}{2}})^2 \omega_0^2}$$
$$+ \frac{1}{8\omega_0} \left(\frac{-5\chi_0^2}{12\omega_0^2} (\boldsymbol{c}^T \boldsymbol{Q} \boldsymbol{c})^2 - 4\left(\frac{1}{64\omega_0^2} \right) \left(\chi_0^2 (f^*)^2 - 16(Ga^{-\frac{1}{2}})^2 \omega_0^2 \right) \right), \qquad (46a)$$

$$\omega = \omega_0 - \frac{1}{8\omega_0} \sqrt{\chi_0^2 (f^*)^2 - 16(Ga^{-\frac{1}{2}})^2 \omega_0^2}$$
$$+ \frac{1}{8\omega_0} \left(\frac{\chi_0^2}{12\omega_0^2} (\boldsymbol{c}^T \boldsymbol{Q} \boldsymbol{c})^2 - 4\left(\frac{1}{64\omega_0^2} \right) \left(\chi_0^2 (f^*)^2 - 16(Ga^{-\frac{1}{2}})^2 \omega_0^2 \right) \right). \qquad (46b)$$

Note the explicit dependence of the linear forcing term f^* on the shape of the harmonic tongues.

IV. RESULTS

We compute the shape of the instability tongues using both Floquet theory and our perturbation method and show how they depend upon the dimensionless parameters. For both methods, we typically use $N = 4$ and $L = 20$ in our computations to ensure accuracy and convergence of the shape of the first two instability tongues. Each instability tongue, both subharmonic and harmonic, is defined by spatial structure of the interface shape. Figure 4 illustrates the modal structure by plotting typical $(a - c)$ interface shapes and $(d - f)$ corresponding wave slopes. Each shape is defined by the mode number pair (n, m), where the azimuthal mode number m represents the number of polar sectors, and the radial mode number n represents the number of nodes, or locations of zero displacement in the radial direction. More details regarding how to identify modes from the wave slope images are given in Shao et al.[1]

A. Axisymmetric m=0 modes

We begin with the axisymmetric $m = 0$ modes and verifying our model predictions against prior experimental results.[1] Figure 5 plots the subharmonic tongues for the [1, 0] and [2, 0] modes and compares with experiments of Ref. 1 (black $*$ s) for $Bo = 167$ and $h = 0.628$. The agreement between both methods (Floquet and perturbation) with experiment is excellent.

Figure 6 plots the harmonic and subharmonic instability tongues for the first two axisymmetric, (1, 0) and (2, 0), modes. Note that both the harmonic and subharmonic tongues with pinned contact line are shifted to higher frequency relative to the free contact line, while the shape of the tongue is largely unaffected. This can be explained by noting that the pinned contact line is more constrained than the free contact line leading to a larger resonance frequency, which can be identified from the instability tongue as the frequency ω with smallest threshold acceleration χ_0. For an inviscid liquid $Ga^{-1/2} = 0$, the threshold acceleration is zero. The variation in the shape of the instability tongues with the contact angle θ_0 is very small for the large Bond numbers $Bo \geq 100$ we consider here and we do not consider these effects any further.
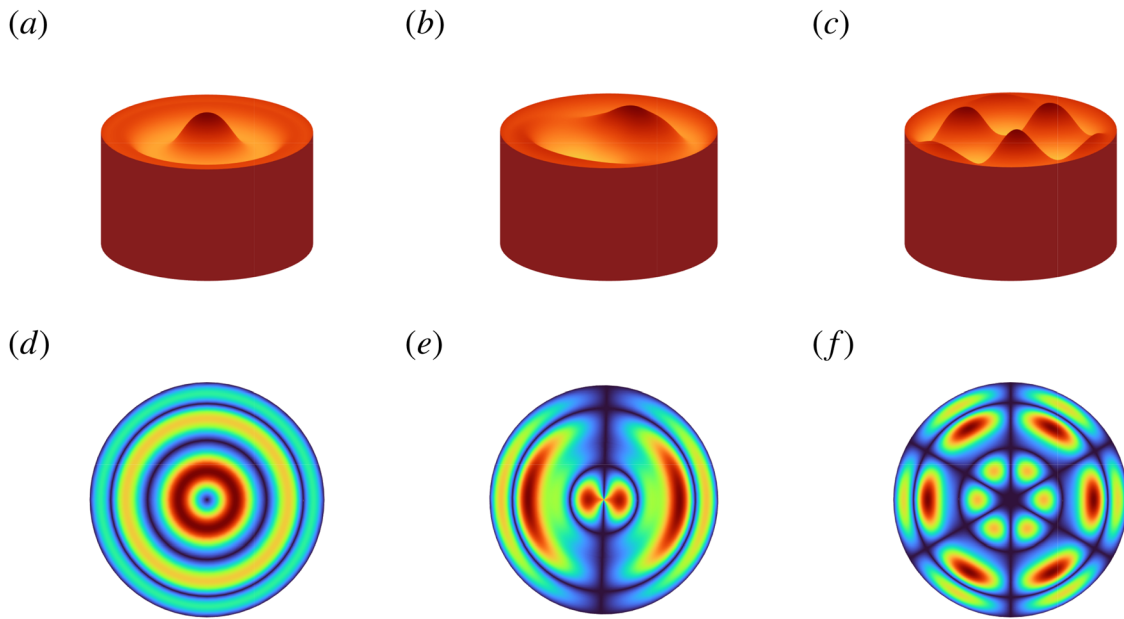
14 November 2024 18:31:10

FIG. 4. Mode (n, m) shape predictions plotting the (a)–(c) surface shape and (d)–(f) corresponding wave slope image for the (a) and (d) $(2, 0)$, (b) and (e) $(2, 1)$, and (c) and (f) $(2, 3)$ modes.

The shape of the harmonic tongues for the axisymmetric modes depends upon f^*. We begin by treating f^* as a fitting parameter. Figure 7(a) plots the instability tongues for the $(1, 0)$ mode with pinned contact-line showing how f^* affects the shape of the tongue. Recall that only the axisymmetric modes with a meniscus $\theta_0 \neq 90°$ are affected by f^*. It is interesting to note that the shape of tongue is governed by the quadratic term $\mathcal{O}(\chi_0^2)$ when $f^* = 0$. In contrast, for $f^* \neq 0$, the shape of tongue is dominated by the linear term $\mathcal{O}(\chi_0)$, which tends to make the tongue more symmetric. The tongue is nearly

FIG. 5. Verification of the shape of the subharmonic tongues for the $(1, 0)$ and $(2, 0)$ modes with pinned contact line predicted by Floquet theory and the perturbation method by comparing against the experiments of Ref. 1—Fig. 4. Here $Ga^{-\frac{1}{2}} = 0$, $Bo = 167$, $h = 0.628$, and $\theta_0 = 90°$.

symmetric when $f^* = 10$ especially for small χ_0. There is a crossover effect when $f^* = 1$, where the detuning force term and the parametric term compete against each other giving rise to the unique tongue shape, which has also been reported in the double parametric forcing system.[57,58] Figure 7(b) plots the instability tongues for a weakly viscous liquid $Ga^{-1/2} = 0.001$. Here, the effect of increasing f^* is to widen the harmonic tongue and shift it lower, such that when $f^*_{\min} = 0.268$ the threshold amplitude for the harmonic tongue is lower than that for the subharmonic tongue. In addition, the threshold acceleration for the harmonic tongue is $\chi_0 = 0.00093$ when $f^* = 10$ so that the effect of damping almost cancels.

The instability tongues typically shift higher with increasing mode number $(n, 0)$, as clearly seen in the subharmonic tongues in Fig. 8. The bandwidth also decreases with increasing mode number for the harmonic tongues, as shown in Fig. 9(a). Viscosity $Ga^{-\frac{1}{2}}$ has a more pronounced effect on the higher modes and tends to shift those tongues higher compared with the lower modes, as shown Fig. 9(b). This is consistent with increased viscous dissipation and a lower response amplitude for higher modes compared with lower modes. This implies that higher modes need a large empirical number f^* to counteract this shift higher in threshold acceleration due to viscosity.
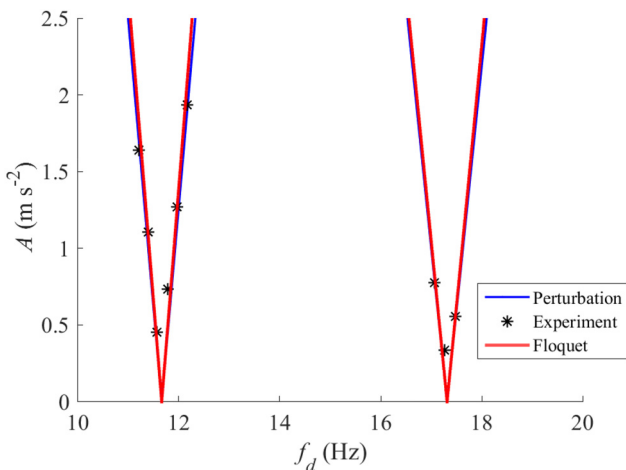
B. Asymmetric $m \neq 0$ modes

The asymmetric $m \neq 0$ modes are governed by the homogeneous system, and the shape of the instability tongues is readily computed by Floquet theory. Figure 10(a) plots the subharmonic tongues for the $(1, 2)$, $(1, 3)$, $(2, 1)$, $(1, 4)$, $(2, 2)$, $(1, 5)$, $(2, 3)$, and $(1, 6)$ modes to compare against experiments by Shao et al.,[1] who also showed that all asymmetric $m \neq 0$ modes exhibited a subharmonic response in experiment, regardless of meniscus shape. This is consistent with Eq. (33). Figure 10(b) plots the instability tongues for the asymmetric $(1, 1)$ and
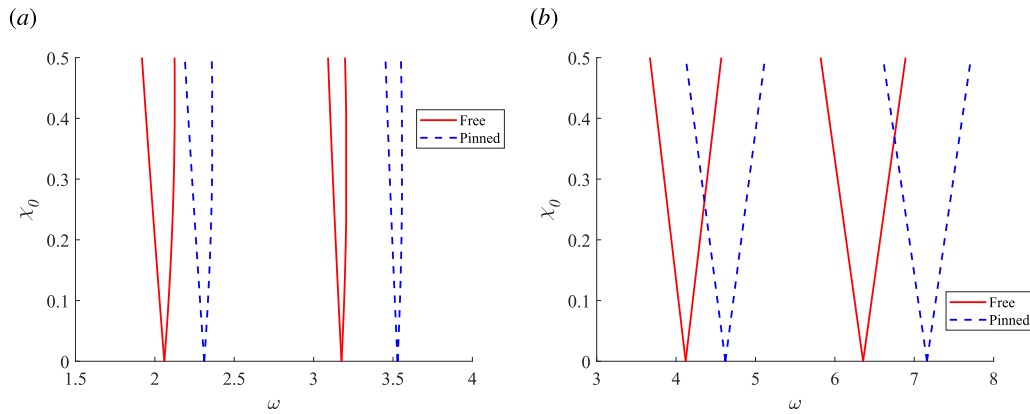
FIG. 6. (a) Harmonic and (b) subharmonic instability tongues for the $(1,0)$ and $(2,0)$ modes plotted in the acceleration-frequency $(\chi_0 - \omega)$ space, contrasting pinned and free contact line conditions. Here $Bo = 100$, $h = 1$, $Ga^{-1/2} = 0$, $\theta_0 = 45°$, and $f^* = 5$.

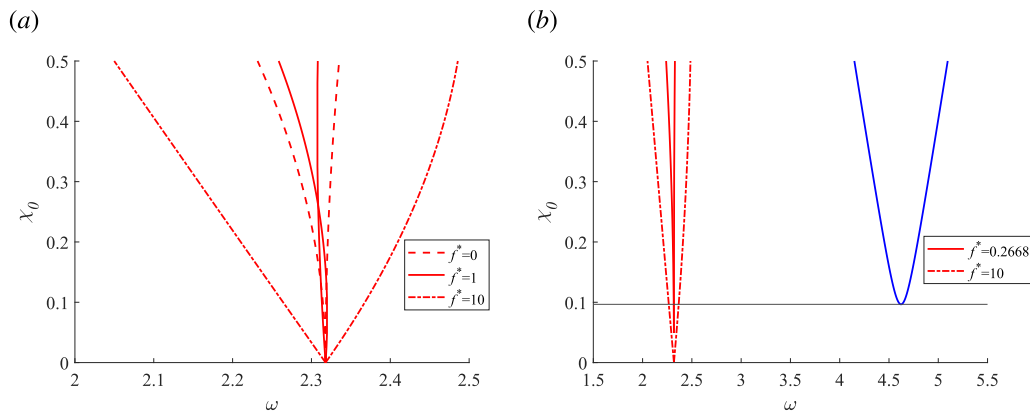**FIG. 7.** (a) Harmonic instability tongues for the $(1,0)$ mode with pinned contact line plotted in the acceleration-frequency $(\chi_0 - \omega)$ space, as they depend upon the empirical number f^*. Here $Bo = 100$, $h = 1$, $Ga^{-1/2} = 0$, and $\theta_0 = 45°$. (b) Harmonic (red line type) and subharmonic (blue line type) instability tongues for the $(1,0)$ mode with pinned contact line plotted in the acceleration-frequency $(\chi_0 - \omega)$ space, as they depend upon the empirical number f^*. Here $Bo = 100$, $h = 1$, $Ga^{-1/2} = 0.001$, and $\theta_0 = 45°$. The black line indicates threshold acceleration χ_0 for the subharmonic tongue.
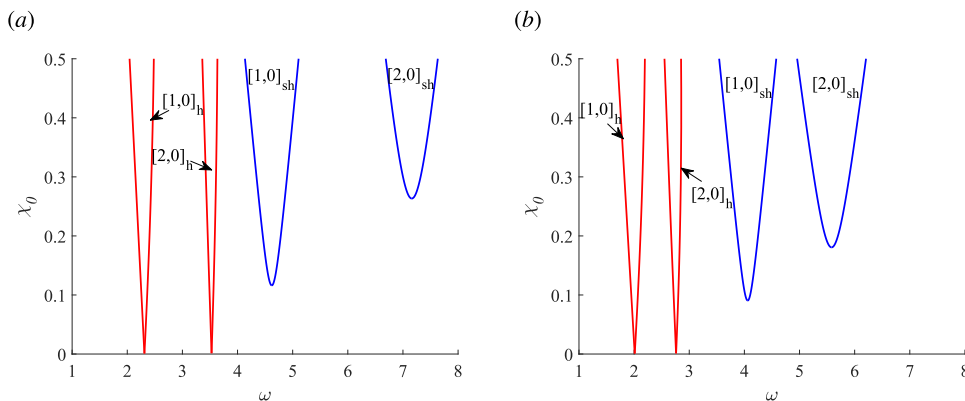

FIG. 8. Harmonic (red line type) and subharmonic (blue line type) instability tongues for the $(1,0)$ and $(2,0)$ modes with pinned contact line plotted in the acceleration-frequency $(\chi_0 - \omega)$ space for (a) $Bo = 100$ and (b) $Bo = 1000$. Here $f^* = 10$, $h = 1$, $Ga^{-\frac{1}{2}} = 0.001$, and $\theta_0 = 45°$.
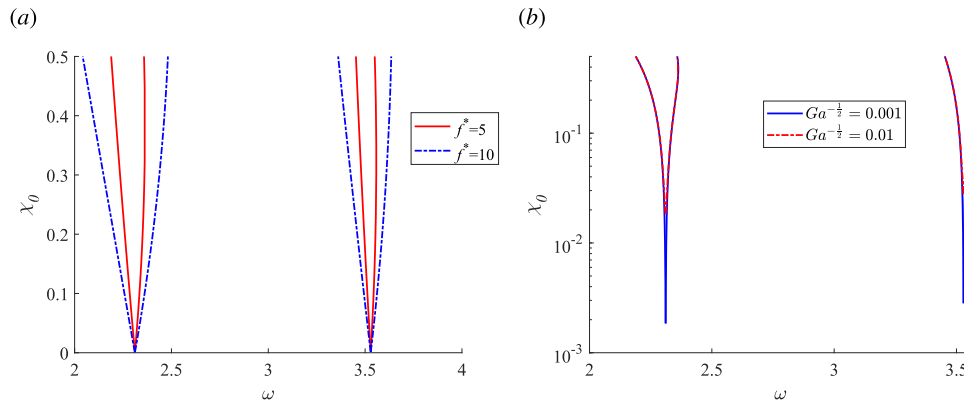
FIG. 9. Harmonic instability tongues for the $(1,0)$ and $(2,0)$ modes with pinned contact line as they depend upon (a) the empirical number f^* for $Ga^{-\frac{1}{2}} = 0.001$ and (b) $Ga^{-\frac{1}{2}}$ for $f^* = 5$. Here $h = 1$, $Bo = 100$, and $\theta_0 = 45°$.
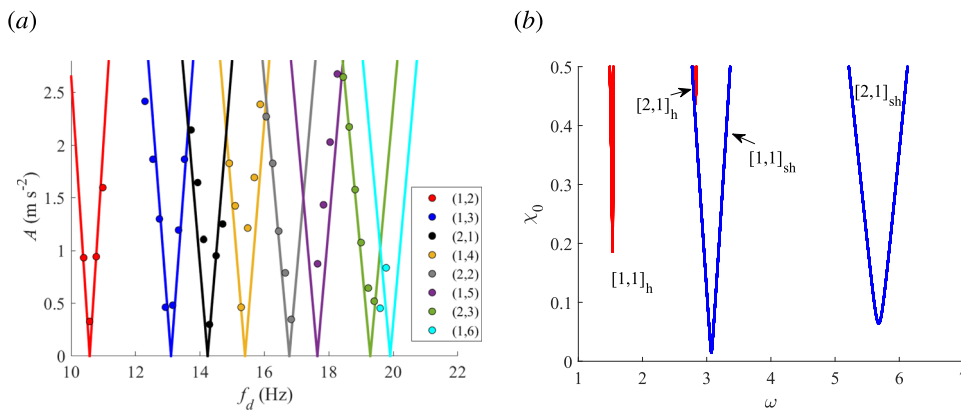

FIG. 10. Instability tongues for asymmetric $m \neq 0$ modes. (a) Comparison of the subharmonic instability tongues for the pinned modes with experiments by Shao et al. (Ref. 1—Fig. 4). (b) Contrasting the harmonic (red line type) and subharmonic (blue line type) instability tongues for the $(1,1)$ and $(2,1)$ modes with pinned contact line in the acceleration-frequency $(\chi_0 - \omega)$ space for $Bo = 100$, $Ga^{-1/2} = 0.001$, $h = 1$, and $\theta_0 = 45°$.

$(2,1)$ modes. Here, the subharmonic tongues always have lower threshold acceleration χ_0 than the harmonic tongues, suggesting that it is easier to excite subharmonic asymmetric modes, also consistent with experiment.[1]

C. Mode mixing

As discussed in the Introduction, Shao et al.[1] reported the experimental observation of mixing modes, where it is possible to simultaneously excite an axisymmetric $m = 0$ mode harmonically and an asymmetric $m \neq 0$ mode subharmonically with the same driving frequency by creating a meniscus and increasing the forcing amplitude above the Faraday wave threshold, as illustrated in Fig. 1(c). This experimental observation was a major motivation for this theoretical study and we illustrate how our results are consistent with those experiments. Figure 11 plots the harmonic instability tongue for the $(9,0)$ mode and the subharmonic instability tongue for the $(6,3)$ mode with parameter values consistent with the experimental values reported by Shao et al. (Ref. 1, Fig. 8). For a fixed driving frequency $f_d = 34.7$ Hz (vertical line in Fig. 11), as you increase the driving amplitude A, a harmonic $(9,0)$ mode is excited after the threshold acceleration for the corresponding harmonic tongue is reached. Increasing the driving amplitude even further excites a subharmonic
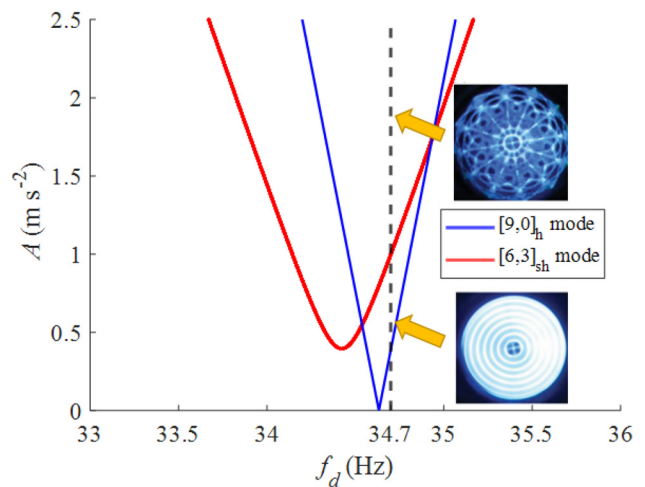

FIG. 11. Illustration of mode mixing by plotting the $(9,0)$ harmonic and $(6,3)$ subharmonic instability tongues in the acceleration-driving frequency $A - f_d$ space for $Ga^{-\frac{1}{2}} = 0.0001$, $Bo = 167$, and $h = 0.628$ to compare with experimental observation of Ref. 1—Fig. 8. Reproduced with permission from Shao et al., J. Fluid Mech. **915**, A19 (2021). Copyright 2021 Cambridge University Press.

$(6, 3)$ mode once the threshold acceleration for that subharmonic tongue is reached. Incremental increases in driving amplitude result in the high-amplitude pattern shown in the figure. This interpretation of our theoretical predictions corresponds to the exact mode mixing observed by Shao *et al.* (Ref. [1], Fig. 9), suggesting that our model includes the essential physics to understand this complex phenomena.

V. CONCLUDING REMARKS

We have developed a theoretical model of surface waves on a liquid bath in a vertically vibrated cylindrical container, which couples the meniscus wave formed at the container sidewall to the parametric Faraday wave, as motivated by recent experimental observations of complex spatiotemporal wave behavior in this system.[1] Detuning the driving acceleration of the container gives rise to an inhomogeneous Mathieu equation for axisymmetric $m = 0$ waves, which is distinguished from traditional studies of Faraday waves by the additional linear forcing term on the right hand side of the governing equation. In contrast, asymmetric $m \neq 0$ waves satisfy a standard homogeneous Mathieu equation, highlighting the complex relationship between the spatial wave structure and the temporal response. The shape of the instability tongues was computed by the Floquet theory for asymmetric $m \neq 0$ waves and a perturbation method for axisymmetric $m = 0$ waves. The empirical number f^* is related to the shape of the meniscus and only changes the shape of the harmonic tongues for the axisymmetric modes by decreasing the threshold acceleration χ_0 and increasing the bandwidth. For a range of $f^* > 0$, the threshold acceleration for the axisymmetric $m = 0$ harmonic tongues can be lower than the subharmonic tongues, which is consistent with experimental observations of harmonic edge waves at low driving amplitudes. For a perfectly flat meniscus, the subharmonic tongues always have smaller threshold acceleration than the harmonic tongues, also consistent with experimental observation. Finally, we show how our model can predict the mixing of an axisymmetric $m = 0$ harmonic mode with an asymmetric $m \neq 0$ subharmonic mode at a single driving frequency and compare against experimental results (Ref. [1], Fig. 8). The consistency and great agreement with prior experimental results suggests that our model captures the essential features of these complex spatiotemporal wave patterns.

Our model could be extended to include viscoelastic effects[13,51] and dynamic contact line effects (e.g., by incorporating the Hocking condition).[59] In addition, a number of the experimental observations by Shao *et al.*[1] that motivated our study can also be observed in vertically vibrated sessile drops.[20,60,61] One could apply similar ideas for modeling meniscus effects to that problem, with the understanding that base state curvature of the drop is global whereas the meniscus effects we consider here are localized to the contact line region. From an application point of view, our model could be used as a design tool for pattern formation of the complicated mixed modes.

ACKNOWLEDGMENTS

AUTHOR DECLARATIONS
Conflict of Interest

The authors have no conflicts to disclose.

Author Contributions

D. Ding: Formal analysis (lead); Investigation (lead); Writing – original draft (lead). **J. B. Bostwick:** Conceptualization (lead); Funding acquisition (lead); Supervision (lead); Writing – review & editing (lead).

DATA AVAILABILITY

The data that support the findings of this article are available within the article.

REFERENCES

[1]X. Shao, P. Wilson, J. Saylor, and J. Bostwick, "Surface wave pattern formation in a cylindrical container," J. Fluid Mech. **915**, A19 (2021).

[2]M. Faraday, "XVII. On a peculiar class of acoustical figures; and on certain forms assumed by groups of particles upon vibrating elastic surfaces," Philos. Trans. R. Soc. London **121**, 299–340 (1831).

[3]P. Wright and J. Saylor, "Patterning of particulate films using faraday waves," Rev. Sci. Instrum. **74**, 4063–4070 (2003).

[4]S. Strickland, M. Shearer, and K. Daniels, "Spatiotemporal measurement of surfactant distribution on gravity–capillary waves," J. Fluid Mech. **777**, 523–543 (2015).

[5]A. James, M. Smith, and A. Glezer, "Vibration-induced drop atomization and the numerical simulation of low-frequency single-droplet ejection," J. Fluid Mech. **476**, 29–62 (2003).

[6]B. Vukasinovic, M. Smith, and A. Glezer, "Mechanisms of free-surface breakup in vibration-induced liquid atomization," Phys. Fluids **19**, 012104 (2007).

[7]S. Tsai, S. Lin, R. Mao, and C. Tsai, "Ejection of uniform micrometer-sized droplets from faraday waves on a millimeter-sized water drop," Phys. Rev. Lett. **108**, 154501 (2012).

[8]A. Guex, N. Di Marzio, D. Eglin, M. Alini, and T. Serra, "The waves that make the pattern: A review on acoustic manipulation in biomedical research," Mater. Today Bio **10**, 100110 (2021).

[9]T. B. Benjamin and F. J. Ursell, "The stability of the plane free surface of a liquid in vertical periodic motion," Proc. R. Soc. London, Ser. A **225**(1163), 505–515 (1954).

[10]L. Rayleigh, "VII. On the crispations of fluid resting upon a vibrating support," London, Edinburgh, Dublin Philos. Mag. J. Sci. **16**, 50–58 (1883).

[11]L. Matthiessen, "Akustische versuche, die kleinsten transversalwellen der flüssigkeiten betreffend," Ann. Phys. **210**, 107–117 (1868).

[12]L. Matthiessen, "Ueber die transversalschwingungen tönender tropfbarer und elastischer flüssigkeiten," Ann. Phys. **217**, 375–393 (1870).

[13]X. Shao, P. Wilson, J. Bostwick, and J. Saylor, "Viscoelastic effects in circular edge waves," J. Fluid Mech. **919**, A18 (2021b).

[14]X. Shao, C. Gabbard, J. Bostwick, and J. Saylor, "On the role of meniscus geometry in capillary wave generation," Exp. Fluids **62**, 1–4 (2021c).

[15]K. Kumar and L. Tuckerman, "Parametric instability of the interface between two fluids," J. Fluid Mech. **279**, 49–68 (1994).

[16]K. Kumar, "Linear theory of Faraday instability in viscous liquids," Proc. R. Soc. London, Ser. A **452**(1948), 1113–1126 (1996).

[17]W. Edwards and S. Fauve, "Patterns and quasi-patterns in the faraday experiment," J. Fluid Mech. **278**, 123–148 (1994).

[18]R. Kidambi, "Inviscid faraday waves in a brimful circular cylinder," J. Fluid Mech. **724**, 671–694 (2013).

[19]H. Müller, H. Wittmer, C. Wagner, J. Albers, and K. Knorr, "Analytic stability theory for faraday waves and the observation of the harmonic surface response," Phys. Rev. Lett. **78**, 2357 (1997).

[20]C. Chang, J. Bostwick, P. Steen, and S. Daniel, "Substrate constraint modifies the Rayleigh spectrum of vibrating sessile drops," Phys. Rev. E **88**, 023015 (2013).

[21]S. Douady, "Experimental study of the faraday instability," J. Fluid Mech. **221**, 383–409 (1990).

[22]D. Henderson and J. Miles, "Single-mode faraday waves in small cylinders," J. Fluid Mech. **213**, 95–109 (1990).

[23]F. Batson, W. Zoueshtiagh, and R. Narayanan, "The faraday threshold in small cylinders and the sidewall non-ideality," J. Fluid Mech. **729**, 496–523 (2013).

[24] B. Christiansen, P. Alstrøm, and M. Levinsen, "Dissipation and ordering in capillary waves at high aspect ratios," J. Fluid Mech. **291**, 323–341 (1995).

[25] J. Bechhoefer, V. Ego, S. Manneville, and B. Johnson, "An experimental study of the onset of parametrically pumped surface waves in viscous fluids," J. Fluid Mech. **288**, 325–350 (1995).

[26] A. Bongarzone, F. Viola, S. Camarri, and F. Gallaire, "Subharmonic parametric instability in nearly brimful circular cylinders: A weakly nonlinear analysis," J. Fluid Mech. **947**, A24 (2022).

[27] C. Tipton, *Interfacial Faraday Waves in a Small Cylindrical Cell* (The University of Manchester, Manchester, UK, 2003).

[28] D. Younesian, E. Esmailzadeh, and R. Sedaghati, "Asymptotic solutions and stability analysis for generalized non-homogeneous Mathieu equation," Commun. Nonlinear Sci. Numer. Simul. **12**, 58–71 (2007).

[29] D. Henderson and J. Miles, "Surface-wave damping in a circular cylinder with a fixed contact line," J. Fluid Mech. **275**, 285–299 (1994).

[30] C. Martel, J. Nicolas, and J. Vega, "Surface-wave damping in a brimful circular cylinder," J. Fluid Mech. **360**, 213–228 (1998).

[31] S. Davis, "Moving contact lines and rivulet instabilities. Part 1. The static rivulet," J. Fluid Mech. **98**, 225–242 (1980).

[32] J. Bostwick and P. Steen, "Stability of constrained capillary surfaces," Annu. Rev. Fluid Mech. **47**, 539–568 (2015).

[33] R. Kidambi, "Capillary damping of inviscid surface waves in a circular cylinder," J. Fluid Mech. **627**, 323–340 (2009).

[34] D. Joseph, "Viscous potential flow," J. Fluid Mech. **479**, 191–197 (2003).

[35] S. Ciliberto and J. Gollub, "Pattern competition leads to chaos," Phys. Rev. Lett. **52**, 922 (1984).

[36] S. Ciliberto and J. Gollub, "Chaotic mode competition in parametrically forced surface waves," J. Fluid Mech. **158**, 381–398 (1985).

[37] B. Gluckman, P. Marcq, J. Bridger, and J. Gollub, "Time averaging of chaotic spatiotemporal wave patterns," Phys. Rev. Lett. **71**, 2034 (1993).

[38] H. Müller, "Periodic triangular patterns in the faraday experiment," Phys. Rev. Lett. **71**, 3287 (1993).

[39] H. Arbell and J. Fineberg, "Pattern formation in two-frequency forced parametric waves," Phys. Rev. E **65**, 036224 (2002).

[40] W. Batson, F. Zoueshtiagh, and R. Narayanan, "Two-frequency excitation of single-mode faraday waves," J. Fluid Mech. **764**, 538–571 (2015).

[41] P. Concus, "Static menisci in a vertical right circular cylinder," J. Fluid Mech. **34**, 481–495 (1968).

[42] I. Maksymov and A. Pototsky, "Harmonic and subharmonic waves on the surface of a vibrated liquid drop," Phys. Rev. E **100**, 053106 (2019).

[43] R. Rand, *Lecture Notes on Nonlinear Vibrations* (Cornell University, 2012).

[44] F. Dias, A. I. Dyachenko, and V. E. Zakharov, "Theory of weakly damped free-surface flows: A new formulation based on potential flow solutions," Phys. Lett. A **372**, 1297–1302 (2008).

[45] D. Joseph, "Potential flow of viscous fluids: Historical notes," Int. J. Multiphase Flow **32**, 285–310 (2006).

[46] S. S. Hough, "On the influence of viscosity on waves and currents," Proc. London Math. Soc. **S1-28**, 264–288 (1896).

[47] J. Hunt, "The viscous damping of gravity waves in shallow water," La Houille Blanche **50**, 685–691 (1964).

[48] J. Bostwick and P. Steen, "Dynamics of sessile drops. Part 1. Inviscid theory," J. Fluid Mech. **760**, 5–38 (2014).

[49] D. Ding and J. Bostwick, "Oscillations of a partially wetting bubble," J. Fluid Mech. **945**, A24 (2022).

[50] J. Bostwick and P. Steen, "Capillary oscillations of a constrained liquid drop," Phys. Fluids **21**, 032108 (2009).

[51] P. Wilson, X. Shao, J. Saylor, and J. Bostwick, "Role of edge effects and fluid depth in azimuthal faraday waves," Phys. Rev. Fluids **7**, 014803 (2022).

[52] A. Nayfeh and D. Mook, *Nonlinear Oscillations* (John Wiley & Sons, 2008).

[53] G. Hill, "On the part of the motion of the lunar perigee which is a function of the mean motions of the sun and moon," Acta Math. **8**, 1–36 (1886).

[54] H. Poincaré, *Les Méthodes Nouvelles de la Mécanique Céleste* (Gauthier-Villars et fils, 1899), Vol. 3.

[55] P. Drazin, *Nonlinear Systems, 10* (Cambridge University Press, 1992).

[56] I. Kovacic, R. Rand, and S. Mohamed Sah, "Mathieu's equation and its generalizations: Overview of stability charts and their features," Appl. Mech. Rev. **70**, 020802 (2018).

[57] D. Arrowsmith and R. Mondragóon, "Stability region control for a parametrically forced Mathieu equation," Meccanica **34**, 401–410 (1999).

[58] A. Sofroniou and S. Bishop, "Dynamics of a parametrically excited system with two forcing terms," Mathematics **2**, 172–195 (2014).

[59] L. Hocking, "The damping of capillary–gravity waves at a rigid boundary," J. Fluid Mech. **179**, 253–266 (1987).

[60] C. Chang, J. Bostwick, S. Daniel, and P. Steen, "Dynamics of sessile drops. Part 2. Experiment," J. Fluid Mech. **768**, 442–467 (2015).

[61] P. Steen, C. Chang, and J. Bostwick, "Droplet motions fill a periodic table," Proc. Natl. Acad. Sci. U. S. A. **116**, 4849–4854 (2019).